



OPEN

# Direct fabrication of graphene on SiO<sub>2</sub> enabled by thin film stress engineering

SUBJECT AREAS:

DESIGN, SYNTHESIS AND  
PROCESSING

SYNTHESIS OF GRAPHENE

Daniel Q. McNerny<sup>1</sup>, B. Viswanath<sup>2</sup>, Davor Copic<sup>1</sup>, Fabrice R. Laye<sup>1</sup>, Christophor Prohoda<sup>2</sup>,  
Anna C. Brieland-Shoultz<sup>1</sup>, Erik S. Polsen<sup>1</sup>, Nicholas T. Dee<sup>2</sup>, Vijayen S. Veerasamy<sup>3</sup> & A. John Hart<sup>2</sup><sup>1</sup>Department of Mechanical Engineering, University of Michigan, Ann Arbor, Michigan 48109, <sup>2</sup>Department of Mechanical Engineering, Massachusetts Institute of Technology, Cambridge, Massachusetts 02139, <sup>3</sup>Guardian Industries Corporation, Science and Technology Center, Carleton, Michigan 48117.Received  
3 March 2014Accepted  
6 May 2014Published  
23 May 2014Correspondence and  
requests for materials  
should be addressed to  
A.J.H. (ajhart@mit.  
edu) or V.S.V.  
(vveerasamy@  
guardian.com)

We demonstrate direct production of graphene on SiO<sub>2</sub> by CVD growth of graphene at the interface between a Ni film and the SiO<sub>2</sub> substrate, followed by dry mechanical delamination of the Ni using adhesive tape. This result is enabled by understanding of the competition between stress evolution and microstructure development upon annealing of the Ni prior to the graphene growth step. When the Ni film remains adherent after graphene growth, the balance between residual stress and adhesion governs the ability to mechanically remove the Ni after the CVD process. In this study the graphene on SiO<sub>2</sub> comprises micron-scale domains, ranging from monolayer to multilayer. The graphene has >90% coverage across centimeter-scale dimensions, limited by the size of our CVD chamber. Further engineering of the Ni film microstructure and stress state could enable manufacturing of highly uniform interfacial graphene followed by clean mechanical delamination over practically indefinite dimensions. Moreover, our findings suggest that preferential adhesion can enable production of 2-D materials directly on application-relevant substrates. This is attractive compared to transfer methods, which can cause mechanical damage and leave residues behind.

Recent advances in the growth of graphene by chemical vapor deposition (CVD) have enabled the controlled preparation of graphene films of uniform thickness and high quality, despite their polycrystalline structure and orientation<sup>1</sup>. To realize many of the potential applications of graphene, there remains a need for scalable methods of transferring graphene from the metal film or foil growth substrate, which is often Cu or Ni, to application-specific substrates<sup>2</sup>. Moreover, graphene transfer methods typically require multiple steps, and can damage the graphene and/or degrade its properties such as electron mobility<sup>3–5</sup>.

Graphene is most commonly transferred from the metal growth substrate by depositing a polymer film, such as polymethyl methacrylate (PMMA) or polydimethylsiloxane (PDMS) on top of the graphene. This allows etching of the metal to free the polymer-supported graphene for transfer to the desired surface, followed by mechanical transfer to the target surface<sup>6–8</sup>. Unfortunately, chemical etching and transfer with a polymer support layer can introduce wrinkles, tears, and unintended doping of the graphene while leaving behind polymer residue. Graphene removal from metal has alternatively been achieved by depositing epoxy on the graphene followed by mechanical peeling<sup>9,10</sup>. This approach also requires dissolution of the support, and can result in incomplete transfer. More recent work achieved transfer of graphene from SiC to SiO<sub>2</sub>/Si by via deposition of a stressed Ni film on top of the graphene/SiC after growth, followed by mechanical delamination and transfer of the film stack<sup>11</sup>. This method resulted in a uniform wafer-scale graphene film on the target substrate, but still involved transfer and wet etching of the Ni adhesive layer.

It would be more attractive to fabricate graphene directly onto dielectric substrates, thereby avoiding wet chemical processing and the use of a support layer for transfer. Interestingly, it has been shown that graphene grows at the interface of dielectric substrates and Ni or Cu films, under the same conditions that, simultaneously, result in growth on top of the metal film<sup>12,13</sup>. In a related technique, graphene microribbons have been grown at the boundary between lithographically patterned Ni and SiO<sub>2</sub>, where the edges of the Ni dewet and recede during the CVD process<sup>14</sup>. However, removal of the metal film for these interfacial growth systems still requires a wet etching step. Direct fabrication of graphene on SiO<sub>2</sub> was achieved over small areas by *in situ* dewetting and evaporation of a Cu film, which first acted as the growth substrate<sup>15</sup>. However, this method may be challenging to apply to large-area growth of uniform films, and suffers from contamination due to evaporated metal in the CVD system.

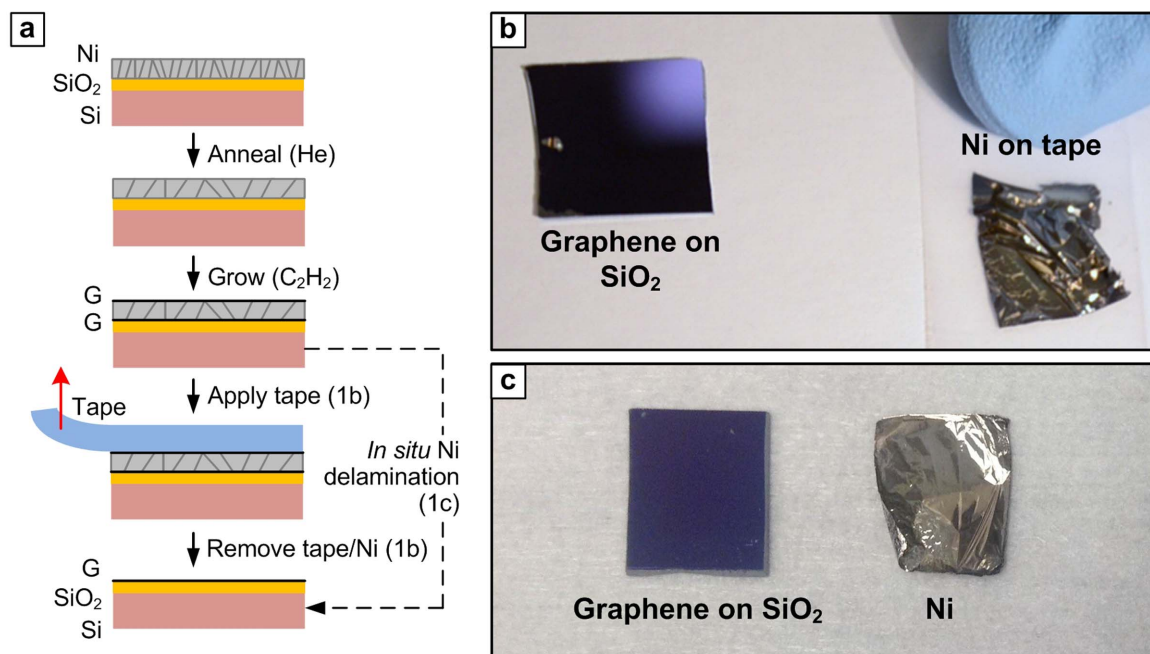


**Figure 1** | Direct fabrication of graphene on SiO<sub>2</sub> by interfacial growth followed by delamination of the Ni film. a) Process schematic, indicating Ni grain growth during annealing in He, followed by graphene growth under CVD conditions, and then removal of Ni using adhesive tape. Photos of substrates ( $\sim 1 \times 1$  cm) and delaminated Ni films in case of b) *ex situ* tape delamination after graphene growth and c) *in situ* delamination during the graphene growth step. In the latter case the Ni film retains its integrity upon delamination and is moved to the side using tweezers after the sample is taken from the CVD system.

We report the direct fabrication of graphene on SiO<sub>2</sub> by growth of interfacial graphene between Ni and SiO<sub>2</sub>, followed by dry mechanical removal of the Ni film from the substrate. This process is enabled by stress engineering of the Ni film along with the reduction adhesion caused by the interfacial graphene layer (IGL). We study the relationship between the microstructure and stress evolution of the Ni film, and find that annealing the film in He prior to graphene growth induces increased stress development. Moreover, the annealing and graphene growth conditions mediate whether the Ni film delaminates *in situ* upon graphene growth, or remains adherent to the substrate after the process.

## Results

**Interfacial graphene layer (IGL) growth by CVD and removal of Ni film.** Direct formation of graphene on SiO<sub>2</sub>, followed by dry removal of Ni, is achieved using Ni thin films with engineered microstructure and stress. The stress in the Ni is controlled by the residual stress from the film deposition process as well as the stress evolution during the annealing of the film prior to graphene growth. Ni films (200 nm) were deposited by e-beam evaporation on (100) Si wafers with 300 nm thermally grown SiO<sub>2</sub>. Graphene growth was performed using a cold-wall quartz tube CVD system, where the sample is placed on a suspended resistively heated Si platform<sup>16</sup>. The system is shown in Supplementary Fig. 1 (Supplementary Information) and an exemplary program of substrate temperature and gas flows is shown in Supplementary Fig. 2. Due to its low thermal mass, the heated platform reaches the process temperature (800–900 °C) in approximately 10 seconds. After heating, the platform is held at constant temperature, typically for 5 minutes. Experiments were performed using He or H<sub>2</sub> as the annealing atmosphere. C<sub>2</sub>H<sub>2</sub> (see Methods) was used as the carbon source for graphene growth, with exposure times ranging from 10–120 seconds. The process was terminated by turning off the heater power, resulting in rapid cooling of the substrate ( $\sim 50$  °C/s). Experiments were performed both at low pressure (2 Torr) and atmospheric pressure; in each case the pressure was kept constant throughout the process.

Via this general CVD method, graphene forms both on the top and bottom (at the Ni/SiO<sub>2</sub> interface) of the Ni film. Graphene growth at the interface is promoted by diffusion of carbon through the Ni and along grain boundaries<sup>12,13</sup>. The adhesion of Ni to the substrate and the presence of a remaining graphene layer on the SiO<sub>2</sub> after Ni film delamination depend on the CVD parameters. As a result, direct transfer of the IGL can be controlled either by *in situ* delamination of the Ni during the carbon exposure step at high temperature, or mechanical delamination of the Ni after cooling and removal of the substrate as shown in Fig. 1c and 1b, respectively. In our system, at atmospheric pressure, the stress-induced delamination of the weakened films often occurs during the growth phase of the CVD process, depositing the IGL on SiO<sub>2</sub> at a steady elevated temperature (Fig. 1c). Films that are annealed and exposed to hydrocarbons at low pressure remain adhered to the substrate yet can be removed cleanly after cooling with Scotch tape, by firmly applying the tape to the cooled sample surface and peeling manually. In this case, the Ni delaminates from the IGL in a single, continuous film (Fig. 1b).

Under low pressure conditions (2 Torr), 5 minutes of He exposure is needed to enable tape delamination after cooling. Experiments using H<sub>2</sub> annealing at low pressure did not enable tape delamination of the Ni, while atmospheric pressure conditions enabled partial delamination of Ni (i.e., patches remained adhered to the substrate) using tape. However, when the process involved annealing in H<sub>2</sub> rather than He, graphene did not remain on the SiO<sub>2</sub> after delamination of Ni. This suggests that He annealing is vital to control the stress and microstructure of the Ni film and adhesion of the IGL, which is discussed in detail later. X-ray photoelectron spectroscopy was used to quantify the surface composition after Ni delamination using tape, and we found a trace remnant of Ni (0.35%, Supplementary Fig. 3) remaining on the SiO<sub>2</sub>.

Optical imaging of the SiO<sub>2</sub> after Ni delamination (Supplementary Fig. 4) shows a clean surface with features appearing  $\sim 1$ – $2$   $\mu$ m in size. Because of the small domain size and the frequency of wrinkles and edges as discussed below, we did not find it possible to judge the number of layers based on optical images. Therefore, confocal



Raman spectroscopy was used to quantify the coverage and quality of the IGL adhered on SiO<sub>2</sub> after removal of the Ni film (Fig. 2). The graphene on SiO<sub>2</sub> displays the most recognized characteristic peaks: the G band (~1590 cm<sup>-1</sup>), D band (~1338 cm<sup>-1</sup>), and the 2D band (~2660 cm<sup>-1</sup>). 2-dimensional Raman mapping gives an average 2D/G integrated peak ratio ( $I_{2D}/I_G$ ) of ~0.57 and average D/G integrated peak ratio ( $I_D/I_G$ ) of ~0.13, with full coverage over the substrate. Over 70% of the mapped area displays  $I_D/I_G < 0.2$ , indicating high quality and uniformity of the IGL. The FWHM of the G and 2D are ~26 cm<sup>-1</sup> and ~40 cm<sup>-1</sup>, respectively. The narrow FWHM of the 2D peak without the accompanying high  $I_{2D}/I_G$  suggests a misaligned orientation between graphene layers<sup>17</sup>. Additional overtone and combination mode features<sup>18–20</sup> are observed including M (1750 cm<sup>-1</sup>) and iTOLA (1950 cm<sup>-1</sup>) combination modes, G\* (2450 cm<sup>-1</sup>), G + D (2950 cm<sup>-1</sup>), and 2D' (3240 cm<sup>-1</sup>). Raman maps of the G, D and 2D bands are shown in Supplementary Fig. 5.

We make two further striking observations, namely, splitting of the G peak, and asymmetric peak shifts (Fig. 2a). The splitting of the G peak (G<sup>-</sup> at 1570 cm<sup>-1</sup> and G<sup>+</sup> at 1590 cm<sup>-1</sup>) of the IGL is suggestive of strain<sup>21</sup> and/or the zigzag edge structure of the graphene layers<sup>22</sup>. In comparison, graphene examined on the exposed side (top) of the delaminated Ni film does not exhibit splitting of the G peak. For the IGL, a significant blue shift of the 2D peak location is observed, accompanied by a red shift of the split G peak. Strain usually affects the G and 2D peaks in a symmetric manner, suggesting that the shift in our results is due to the interference of multiple effects. Moreover the shift in the G peak of the IGL could also arise due to distance-dependent interactions with the SiO<sub>2</sub>, influencing the local charge density levels of graphene<sup>23</sup>.

Growth of graphene at the Ni/SiO<sub>2</sub> interface is further confirmed by cross sectional TEM imaging. Figure 3a shows a bright field cross-sectional TEM image revealing the thicknesses of the SiO<sub>2</sub> (300 nm) and Ni layers (150 nm). Note that the average film thickness of the Ni reduces from the as-deposited value of 200 nm, due to densification during heat treatment. To resolve the IGL precisely, the cross-sectional specimen was tilted to the [011] zone axis of Si (Supplementary Fig. 6), revealing the lattice fringes shown in Fig. 3b with interlayer distance of 0.352 nm (Fig. 3c).

Plan view TEM was also employed to investigate both the top and interfacial graphene films. Graphene grown on the top surface of the Ni film is apparent from the bright field image showing the lacy carbon structure beneath the graphene layers (Supplementary Fig. 7a). Bilayer and few layer graphene domains are evident from the frequently observed Moiré fringes and SAED pattern containing two sets of six fold pattern with misorientation (Supplementary Fig. 7b). Similar graphene domains grown at the Ni-SiO<sub>2</sub> interface, then removed from the substrate for imaging, are shown in Supplementary Fig. 7c.

AFM characterization of the IGL shows distinct closed wrinkles of ~1 nm height and ~50 nm period (Supplementary Fig. 8a). This closed wrinkle structure matches the microstructure of the Ni film, indicating the formation of wrinkles around the Ni grains. Moreover, the closed wrinkles in the IGL suggest that graphene grows outward from the Ni grains that are pinned against the SiO<sub>2</sub>, and that the wrinkles accumulate at the grain boundaries. Similar closed wrinkles are observed in SEM images of the Ni top surface after graphene growth (Supplementary Fig. 8b). Thermally induced wrinkles (Supplementary Fig. 8c), which form a web-like pattern, are also observed on graphene on top of the delaminated Ni. However, these are not seen in the transferred IGL on SiO<sub>2</sub>/Si. Graphene has negative thermal expansion ( $-8 \times 10^{-6} \text{ K}^{-1}$ ) and therefore expands upon cooling, while both Ni and SiO<sub>2</sub>/Si substrates have positive thermal expansions, and therefore shrink upon cooling from the growth temperature. The thermal expansion coefficient of Ni is at least five times that of Si, causing graphene grown on Ni to develop a greater

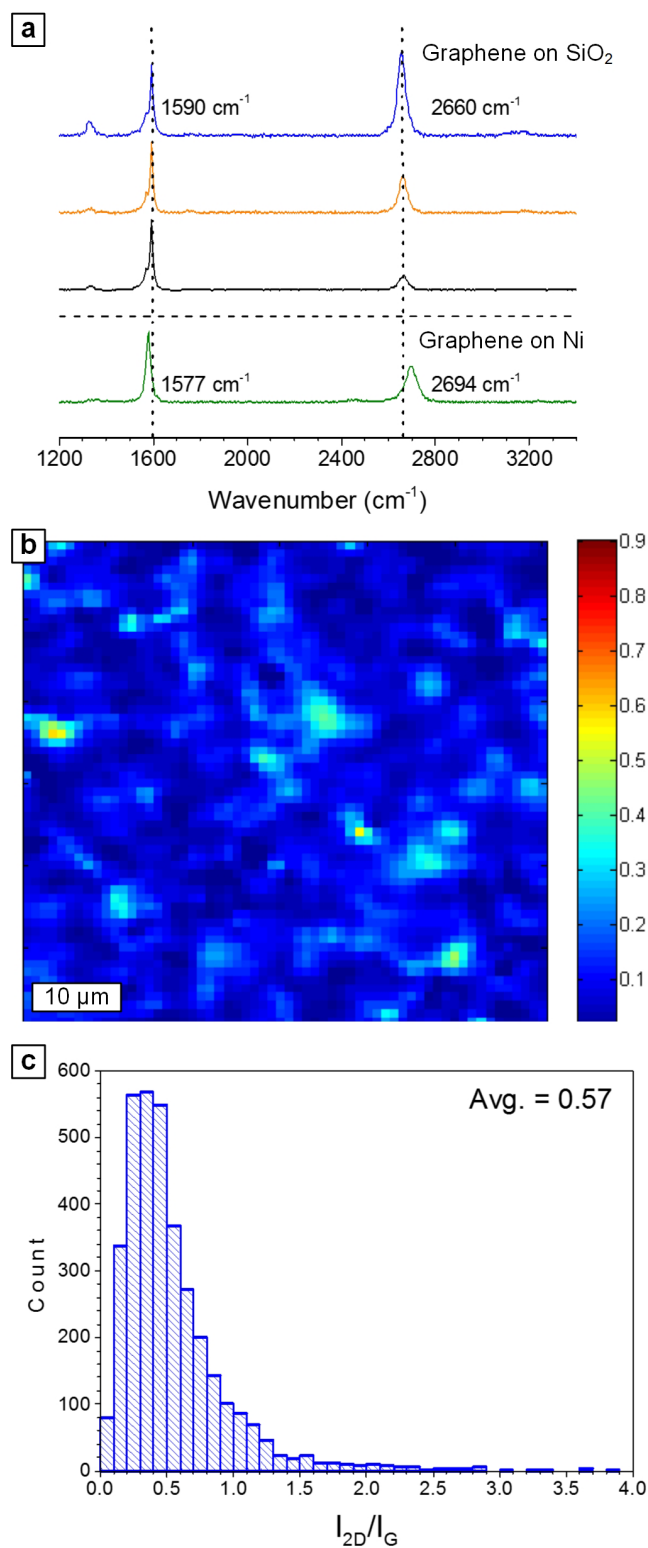


**Figure 2 | Raman spectroscopy of graphene on SiO<sub>2</sub> after tape delamination of Ni.** a) Single pixel Raman spectra of graphene on SiO<sub>2</sub> (blue, orange, and black), compared to graphene grown on the top surface of the same Ni film (green). Graphene on SiO<sub>2</sub> displays a significant blue shift of the 2D peak location accompanied by a splitting and red shift of the split G peak. b) 2-D Raman mapping shows uniform coverage and quality (average  $I_D/I_G = 0.13$ ) across the substrate c) histogram from the  $I_{2D}/I_G$  map suggests that graphene domains range from one to several layers.

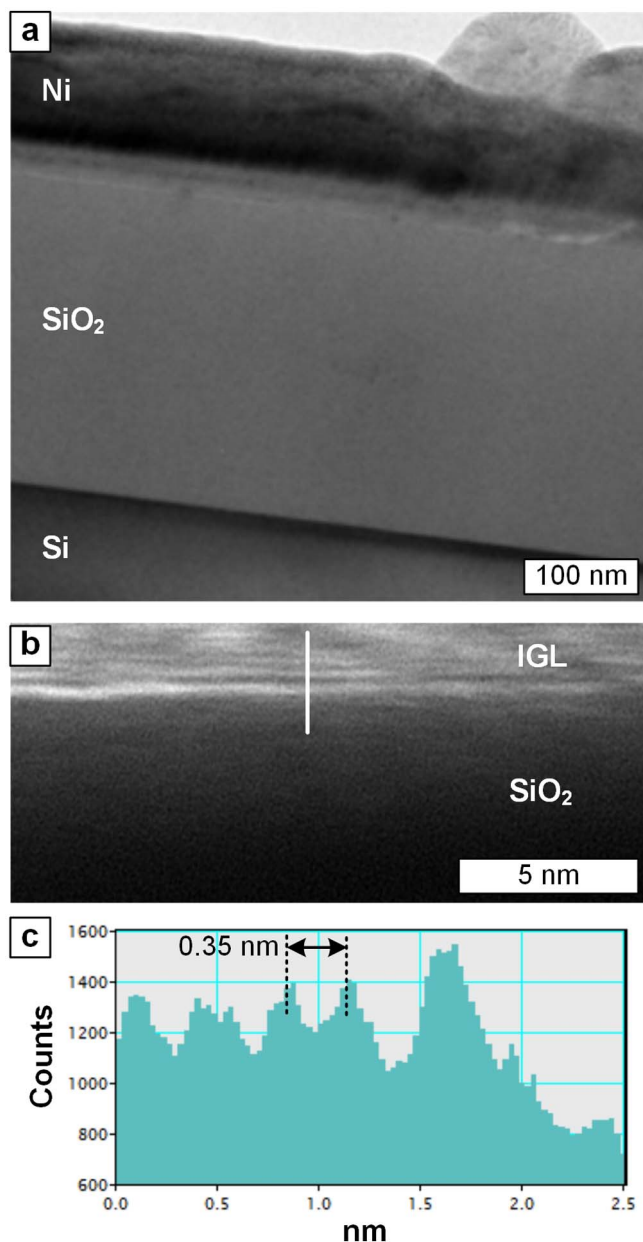


**Figure 3** | TEM analysis of interfacial graphene layers (IGL). a) Cross sectional bright-field TEM and b) HRTEM images of graphene grown at the Ni/SiO<sub>2</sub> interface. c) The line intensity profile across the SiO<sub>2</sub>-IGL interface, corresponding to the line drawn in (b) resolves the graphene interlayer spacing of 0.35 nm.

higher compressive stress, which explains why thermal wrinkles are more clearly visible on the top layer graphene on Ni<sup>24</sup>.

The same conditions were used to create self-patterned islands of graphene on SiO<sub>2</sub>. As shown in Fig. 4, we first patterned Ni features by a lift-off process (see Methods), then performed the graphene growth process, then removed the Ni with tape. Arrays (here 30 × 30 μm) of IGL patches of comparable quality and coverage to the non-patterned samples were confirmed by 2-D Raman spectroscopy.

Last, we note that we occasionally observed carbon nanotubes (CNTs) at the boundary of Ni regions that delaminated *in situ*, where Ni particles were created due to dewetting of the Ni film (Supplementary Fig. 9). This is not surprising considering that Ni nanoparticles are frequently used to template CNT growth under hydrocarbon CVD conditions. However, we have exhaustively examined our samples to ensure that this is an isolated effect, and

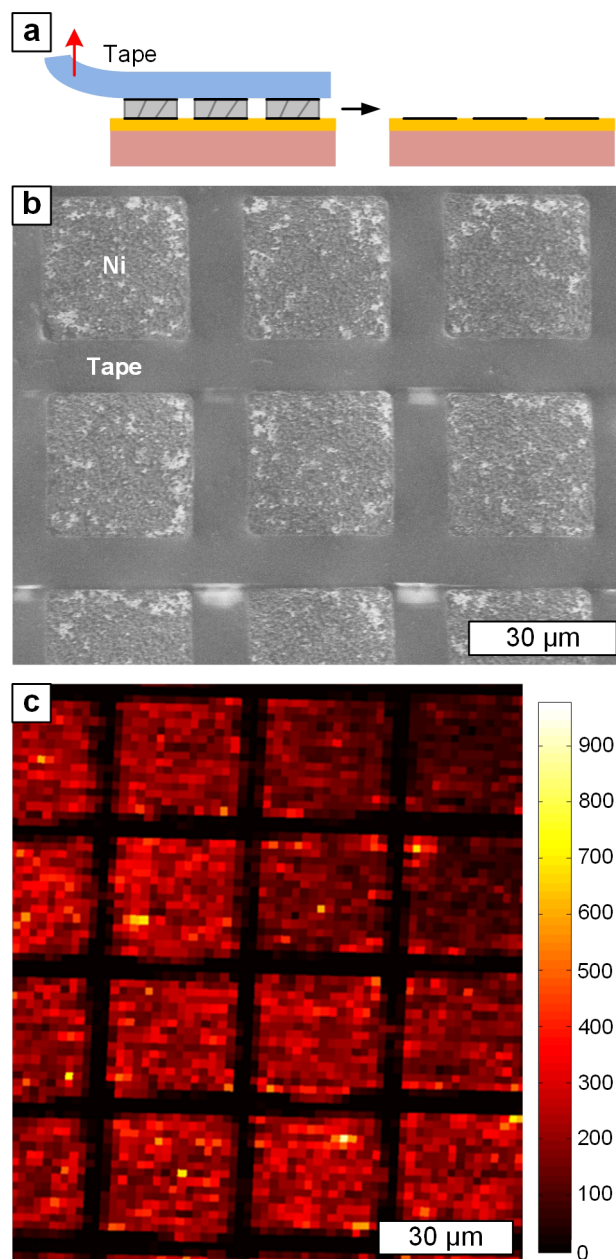


**Figure 4** | Fabrication of micro-scale graphene patterns by tape delamination of pre-patterned Ni, following IGL growth. The schematic in a) shows the tape delamination of Ni leaving the patterned IGL on SiO<sub>2</sub>. b) SEM shows the delaminated Ni patterns on tape while the interfacial graphene on SiO<sub>2</sub> is confirmed by c) 2-D Raman map of I<sub>G</sub>.

moreover do not find CNTs on samples that remain adhered throughout the process and subsequently underwent tape-assisted delamination of the Ni.

**Stress engineering of Ni to enable delamination after graphene growth.** Stress development due to grain growth and microstructure formation within the Ni film during the annealing and graphene growth steps is critical to enable delamination of Ni and adherence of graphene to SiO<sub>2</sub> after the process. The stress development and mechanical integrity of Ni is highly coupled to the deposition parameters, film thickness, thermal expansion mismatch, annealing conditions, and CVD conditions.

The as-deposited Ni film (Fig. 5a) with thickness of 200 nm has a nearly equiaxed grain size of approximately 14 nm. Significant grain



growth and densification are observed after atmospheric pressure annealing in He; after 5 minutes the Ni film has average grain size of approximately 350 nm, and the grains are densely packed (Fig. 5a). SEM images also reveal that annealing in He imparts a high surface area porous microstructure, arising from He trapping and segregation in Ni<sup>25,26</sup>. Annealing in He (Fig. 5b) at low pressure does not cause appreciable grain growth in our Ni films. In comparison, annealing in H<sub>2</sub> (Fig. 5c,d) displays grain growth without the development of a porous microstructure. Therefore, we conclude that annealing the Ni film in He, rather than H<sub>2</sub> as commonly seen in graphene CVD literature<sup>1</sup>, is critical to engineered stress development in the Ni in concert with graphene CVD and stresses induced by grain growth are a significant driving force in whether delamination and transfer occurs *in situ* or can be performed by tape delamination after the CVD process.

To understand the kinetics of grain growth and its influence on stress evolution, systematic rapid thermal annealing experiments were performed (95% He, 5% H<sub>2</sub>). Each experiment involved heating the substrate (1 minute duration), then holding at 875°C for the specified time, and then cooling. The evolution in the Ni film morphology and microstructure with He/H<sub>2</sub> annealing time is shown via optical and SEM images in Supplementary Fig. 10. The average grain size (Fig. 5e) increased from the 14 nm to 341 nm after annealing. There is rapid grain growth at the initial stage and the grain size approaches around 240 nm in less than 1 minute. After this point, grain growth is gradual and the grain size saturates (Fig. 5f).

After annealing times up to 3 minutes, the film is extensively cracked upon cooling, whereas nearly crack-free buckling-induced delamination is seen after longer annealing times (4–5 minutes). Cracking occurs due to increased tensile stress arising from thermal mismatch between the substrate and Ni film during cooling, whereas buckling and delamination occur when annealing at high temperature leads to high compressive stress and weakened coarse grains. However, Ni films annealed in H<sub>2</sub> do not buckle or readily delaminate, although the thermal stress at 875°C is compressive.

## Discussion

To construct a clearer picture of the multivariate relationship that governs stress evolution in Ni, graphene growth, and preferential adhesion of IGL upon Ni delamination, we consider the contributions to stress in the Ni film and the origin of adhesion of Ni to the substrate. The contributions to the net film stress are: (1) stress arising during deposition of Ni onto SiO<sub>2</sub>; (2) stress due to the thermal expansion mismatch between Ni and the substrate; (3) stress induced by He exposure and accumulation during annealing; (4) stress due annealing-induced grain growth; and (5) stress due to the presence of carbon atoms within the Ni lattice during the graphene growth step. The compressive stress development due to the carbon diffusion in the Ni lattice is expected to be negligible (carbon concentration of 0.18% at 900°C). Here, we focus mainly on residual (1), thermal (2) and grain growth stresses (3) for energy release rate estimation. The chemistry and microstructure of the interface governs the adhesion. While grain growth in concert with He accumulation evolves the microstructure and mechanical properties along with the roughness at the Ni/SiO<sub>2</sub> interface, precipitation of the IGL significantly changes the adhesion energy, promoting delamination in concert with the residual stress in the Ni film.

Estimates of the Ni film stress and energy release rate (ERR) versus time through the process are schematically shown in Fig. 6. The actual thermal profile (Fig. 6a) during the process was used as an input to the stress and ERR calculations. To construct this model, the residual stress of as-grown Ni thin films was measured by cantilever deflection (Supplementary Fig. 11). The thermal stress was estimated from the thermal expansion mismatch, and the grain growth stress development during annealing was estimated based on the average grain size determined from SEM observations (Supplementary

Fig. 12)<sup>27</sup>. Initially the as-deposited Ni film relaxes its tensile stress and develops compressive stress during heating, due to the compressive thermal mismatch stress between Ni and the substrate (Supplementary Fig. 13). Further annealing induces grain growth and develops tensile stress in the Ni film. The amount of tensile stress (approximately 1 GPa) development during grain growth is estimated considering the contractive volume strain associated with grain boundary reduction (Supplementary Fig. 14). The redistribution of excess free volume associated with grain boundaries induces biaxial strain in thin film as the grain boundaries are replaced by large crystallites with lower free volume during grain growth<sup>28</sup>.

A balance between compressive thermal stress and tensile grain growth stress thus determines the net stress in Ni when graphene growth occurs (Fig. 6b). This net stress value along with film microstructure determines whether or not the Ni film remains adherent to the substrate during the CVD process. If it does not adhere, it locally buckles and delaminates, whereas if it does adhere, it cracks while cooling. Therefore, the stress evolution can be controlled by choosing the annealing duration. Severe cracking of the Ni film results when sample is cooled after only 2–3 minutes of annealing in He, whereas *in situ* delamination is observed while the sample is annealed for 4–5 minutes. A longer annealing time causes growth of larger grains, and local debonding or delamination at elevated temperature relieves the stress and prevents cracking upon cooling. Operating the process at low pressure (~2 Torr), for both He annealing and graphene growth, slows the kinetics of grain growth and He accumulation, and enables tape-assisted Ni delamination afterwards. In this case, the film remains globally adherent through the process at high temperature, yet local debonding may occur after the interface adhesion weakens. Cracking is prevented during cooling, and the Ni can be removed as a continuous film as shown in Fig. 1.

It is known that the segregation of hydrogen reduces the cohesive strength of grain boundaries and causes intergranular fracture in Ni. However, hydrogen embrittlement is negligible at high temperatures (above 0.45 T<sub>m</sub>) due to its high diffusivity in metals<sup>29</sup>. Using positron annihilation experiments, it has been concluded that micro void formation during He annealing is more effective than H<sub>2</sub> annealing at high temperature because hydrogen-vacancy complexes are unstable above 300°C<sup>30</sup>. In general, the solubility of He in metals is poor and the incorporated He is prone to precipitate into bubbles at high temperatures. Formation of such bubbles leads to drastic changes in the creep and tensile properties causing embrittlement<sup>31</sup>. Interestingly, our SEM observations of Ni films after annealing in He at low pressure (2 Torr) do not reveal any evidence of bubble formation and accelerated grain growth. This stems from decreased He incorporation at low pressure and results in considerably slower microstructural development. In contrast, during the annealing of the Ni film at atmospheric pressure, the He induced bubble density decreases while the grain size increases at the initial stages and is eventually replaced by dense, coarse grain microstructure (Supplementary Fig. 15).

In addition, SEM and TEM imaging of the Ni film annealed in He shows twin boundaries resulting from grain growth where high-energy grain boundaries are replaced by lower energy twin boundaries (Supplementary Fig. 16). Twin boundaries are observed only after 3 minutes of annealing, during the final stage of grain growth proximate to delamination. Because twin boundaries are stronger and accumulate fewer impurities than random grain boundaries, susceptibility to embrittlement is reduced by twin boundaries, increasing the fracture toughness up to 30% in previous work<sup>32</sup>.

To gain further insight about the preferential adhesion of at least some of the graphene layers to SiO<sub>2</sub> upon delamination of the Ni, we surveyed literature on the relative adhesion strengths of the constituent interfaces, e.g., G/Ni, Ni/SiO<sub>2</sub>, and G/G (where G = graphene).

Reported values of G/Ni adhesion range from 0.2–1.5 J/m<sup>2</sup> (averaging 0.71 J/m<sup>2</sup>), determined through quantum DFT and LDA

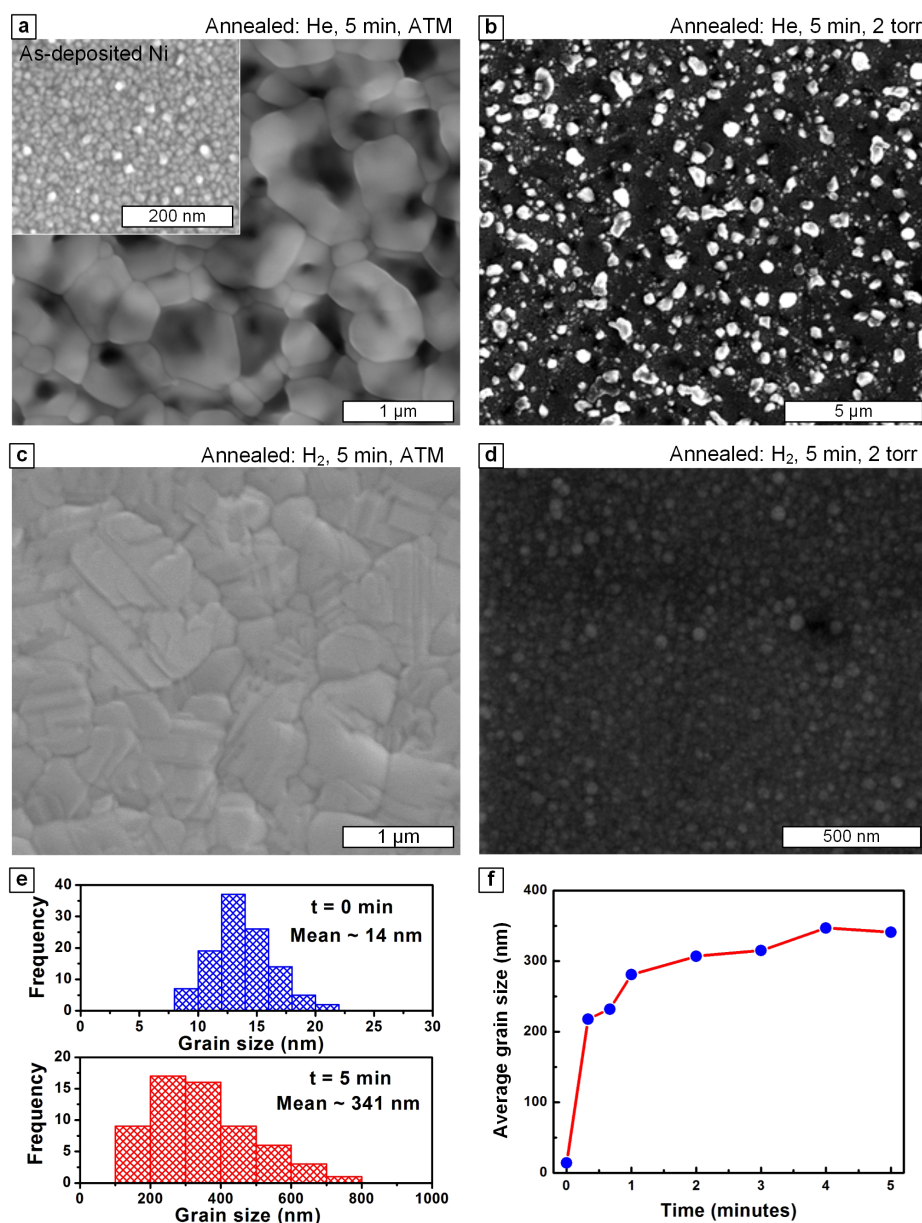


**Figure 5** | Effect of annealing on the microstructure of Ni film deposited on SiO<sub>2</sub> by electron beam evaporation. SEM micrographs of: a) Ni film (200 nm thick) (inset shows as-deposited film) annealed in He, atmospheric pressure; b) annealed in He, 2 Torr; c) annealed in H<sub>2</sub>, atmospheric pressure; d) annealed in H<sub>2</sub> gas pressure, 2 Torr. Significant grain growth is observed when Ni film is annealed at atmospheric pressure. e) Distribution of Ni grain sizes as-deposited, and after 5 minutes in He, at atmospheric pressure. f) Time evolution of average grain size during He annealing, atmospheric pressure. All annealing experiments were done at 875 °C.

computational techniques<sup>33–35</sup>. Interpretation of these numbers in relevance to our study is further complicated by the polycrystallinity of the Ni. Because the Ni(100) surface is energetically less favorable compared to the Ni(111) surface, we can estimate the strength of Ni(100)-graphene adsorption to be approximately 1.6 times that of Ni(111) by considering the variation in adsorption strength of benzene on Ni<sup>36</sup>. Similarly, the adhesion of Ni(111) on crystalline SiO<sub>2</sub>(0001) is much greater (1.29–1.37 J/m<sup>2</sup>), and imposes a mismatch strain of approximately 1%<sup>37</sup>. G/SiO<sub>2</sub> (amorphous) adhesion was found to be 0.45 J/m<sup>2</sup>, and graphene adhesion to the (0001) surface of crystalline SiO<sub>2</sub> was found to be approximately 0.2 times this value<sup>38,39</sup>.

Graphene-graphene adhesion also depends on many factors including the structure, roughness, and crystallinity of both the graphene and substrate, and as a result widely varying values are reported. Taken together, experimental and computational evidence

suggests that G/G adhesion (cohesion) is dependent upon the number of graphene layers, but is generally found to be between 0.1–0.4 J/m<sup>2</sup>, averaging ~0.2 J/m<sup>2</sup><sup>40,41</sup>. Interaction between graphene and the substrate, e.g., when graphene layers are sandwiched by a metal and/or dielectric, can lead to electromagnetic contributions to the G/G adhesion energy<sup>35</sup>.

Therefore, while an accurate quantitative estimate of relative adhesion strengths is out of reach, ordinal trends suggest that G/Ni adhesion is strongest, with G/SiO<sub>2</sub> next, and G/G weakest. We conclude that the graphene remaining on SiO<sub>2</sub> after delamination likely results from separation of multilayer graphene films at the Ni/SiO<sub>2</sub> interface. The existence of multilayer graphene is consistent with the now well-known precipitation mechanism of graphene growth from Ni. Moreover, the polydispersity of layer number shown by 2D Raman spectroscopy suggests that the local contact and delamination conditions determine the number of layers of IGL that remain on SiO<sub>2</sub>.

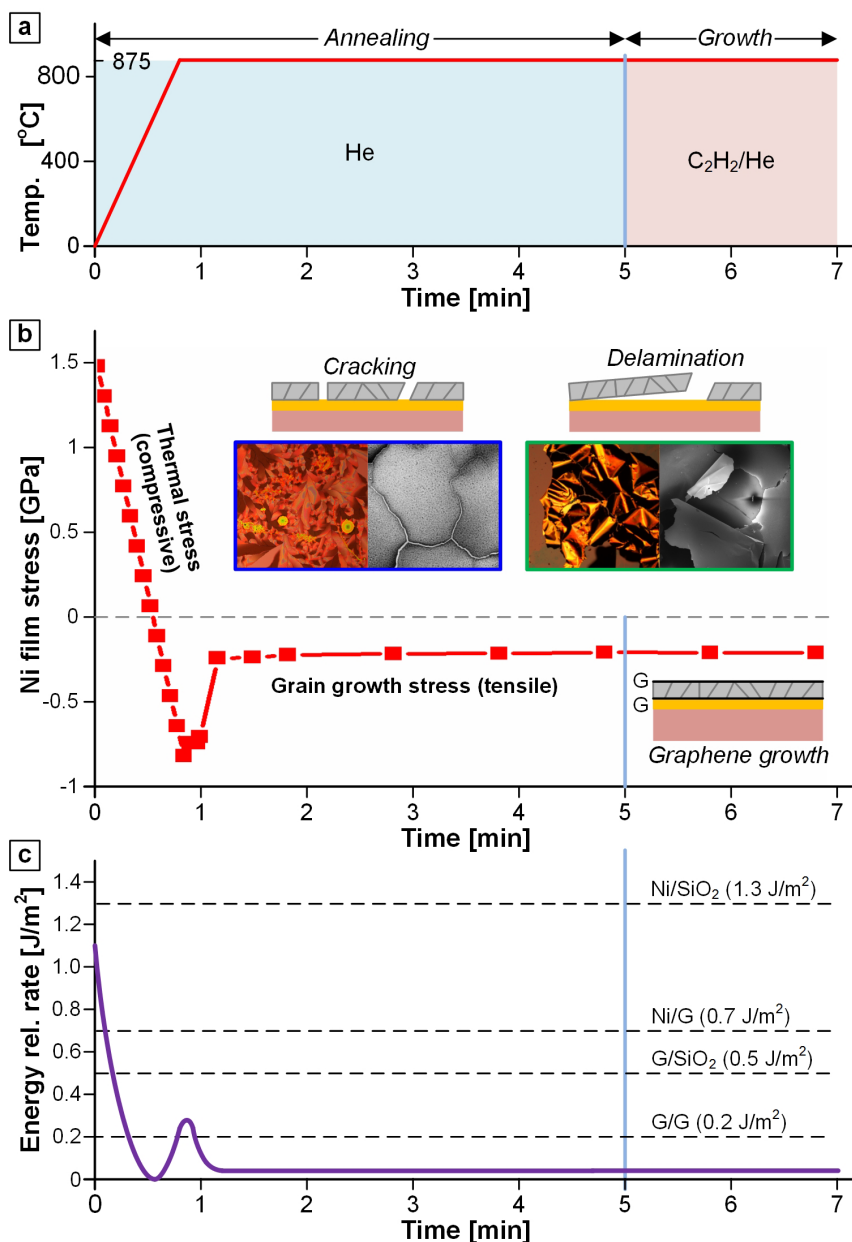


**Figure 6** | Analysis of Ni film stress during annealing and graphene growth. a) Schematic of temperature-time profile. b) Estimated Ni film stress versus time, reflecting competition between thermal stress development during heating followed by grain growth induced tensile stress evolution during annealing. Optical and SEM images of Ni film cracking and delamination observed at different time intervals are shown as insets. c) The corresponding strain energy release rate as a function of processing time is compared with interfacial energies to identify the energetic criterion for Ni film delamination. After the initial transient, the ERR remains below the G/G interfacial energy.

We now construct a plot of energy release rate (ERR) of the Ni film versus time, with reference to the ground state adhesion energies quoted above (Fig. 6c). The continuous variation in stress ( $\sigma_m$ ) is used to estimate net changes in ERR (G) for the constant Ni film thickness ( $h_f$ ), elastic modulus ( $E_f$ ), and Poisson's ratio ( $\nu_f$ ) as,

$$G = \frac{1 - \nu_f^2}{2E_f} \sigma_m^2 h_f. \quad (1)$$

Under the assumptions of our analysis, the initial ERR of 1.17 J/m<sup>2</sup> is estimated from the measured residual stress (1.53 GPa) in 200 nm Ni film. This ERR value is lower than the Ni-SiO<sub>2</sub> interfacial energy and explains the strongly adherent Ni film on SiO<sub>2</sub> in the as-deposited state. During heating, the ERR drops rapidly with time as the tensile residual stress is balanced by the compressive thermal stress developed during rapid heating to 900°C. Further tensile stress

development decreases the ERR and the net ERR eventually reaches a steady state value once the grain growth is saturated.

To facilitate *in situ* delamination of Ni film, the ERR should surpass the G/G interfacial energy ( $\sim 0.2$  J/m<sup>2</sup>) after graphene forms. To facilitate tape delamination after cooling, the ERR should remain below the G/G interfacial energy during the graphene growth step. In both cases, during the annealing process, the ERR should remain below the Ni/SiO<sub>2</sub> interfacial energy to prevent premature delamination. Our estimate of a steady-state ERR of  $\sim 0.05$  J/m<sup>2</sup> after grain growth falls far below the values of Ni/SiO<sub>2</sub>, Ni/G and G/SiO<sub>2</sub> interfacial energies indicating that the delamination at these interfaces is unlikely. The estimated ERR value after the graphene growth stage is comparable to the G/G interfacial energy and yet lower than G/G adhesion, verifying that additional mechanical energy (here provided by the tape-assisted step) is required to fracture the interface after low



pressure growth. At the same time, *in situ* delamination is observed when the growth is carried out at atmospheric pressure as the grain growth exerts tractions at the substrate/thin film interface causing significant local debonding.

Both the ERR and interfacial energies depend on the microstructure of the Ni film, and on the roughness and crystalline character of the interfaces which are not precisely known at this time. Nevertheless, we know annealing Ni in He will promote bubble formation, coalescence and annihilation along with grain growth, weakening the interface. The large grains also will undergo significant strain localization which promotes delamination<sup>42</sup>, whereas the fine grain structure withstands higher stress as its yield strength is far greater than its microcrystalline counterparts. This is partly explained by the Hall–Petch type relationship between the film yield stress and its grain size. Also, the influence of mixed mode interfacial fracture<sup>43</sup> encompassing crack advance at the interface or crack kinking out of the interface on the energy release rate is not considered here as the tape delaminated samples are nearly crack-free.

Notwithstanding these issues, because the estimated ERR falls closely below the G–G interfacial energy, we are confident of the mechanism whereby the G/G interface between SiO<sub>2</sub> and Ni is the weakest interface when multilayer graphene is present. This conclusion is supported by the observation of graphene on both SiO<sub>2</sub> and the bottom of the Ni film after tape delamination (Supplementary Fig. 17). Our estimates also suggest that a single IGL would preferentially adhere to SiO<sub>2</sub> rather than Ni.

We believe that the quality and uniformity of the IGL could be improved significantly in future work. Engineering of larger grain sizes in the Ni, and management of the kinetics of carbon dissolution and precipitation would provide greater control of the graphene structure and number of layers deposited at the interface. The demonstrated process window could be also be tuned by the film thickness, the film–substrate adhesion, and using thermally mismatched substrate–film combinations to vary thin film stresses. For example, we observed *in situ* delamination of Ni during graphene growth at low pressure, upon replacing the He flow with a 95 : 5 He/O<sub>2</sub> flow. This adds moisture to the atmosphere by *in situ* generation of H<sub>2</sub>O<sup>44</sup>. Therefore, moisture intrusion at the graphene and Ni interface may modify the interfacial adhesion of graphene to SiO<sub>2</sub>. As a result, we hypothesize that the moisture levels found at atmospheric conditions may also contribute to the consistent and repeated *in situ* delamination of Ni.

In summary, we have demonstrated that graphene grown at a Ni/SiO<sub>2</sub> interface can be directly retained on a clean SiO<sub>2</sub> substrate by mechanical removal of the Ni after graphene growth or by *in situ* delamination of the Ni at high temperature. This process eliminates the need for post-growth transfer of graphene from metal catalyst films/foils, which are typically lengthy and can result in mechanical and/or chemical damage to the graphene. Control is enabled by engineering the Ni film microstructure and process conditions to balance competition between compressive thermal stress and tensile grain growth stress. Further understanding and control over interfacial graphene growth, and specifically its uniformity and relationship to the metal film grain size, is certainly necessary. With such understanding, this method could be scaled to manufacturing on wafer-scale and larger dimensions, either using blanket Ni films, or pre-patterned Ni shapes to directly template device geometries.

## Methods

**Thin film preparation.** Nickel was deposited on (100) Si wafers with 300 nm thermal SiO<sub>2</sub>, using an e-beam evaporator (Cooke SJ-20). The chamber pressure was lowered to approximately 20 mTorr prior to depositing 200 nm of nickel at 5 Å/s. The wafers were manually scribed and into chips approximately 1 × 1 cm in size. Patterned samples were prepared using standard lithographic processes before nickel deposition, followed by lift-off. The chips with photoresist were placed in a beaker first with acetone and gently agitated for 4 minutes, and then with 2-propanol for 2 minutes.

**Graphene growth.** Graphene growth was achieved using a cold-wall CVD system (modified SabreTube, Absolute Nano LLC). Substrates were placed on an electrically conductive p-doped Si substrate (Supplementary Fig. 1). The reactor was sealed, purged, and the flow of annealing gas (400 sccm), which was He (>99.999%) or H<sub>2</sub> (>99.999%), was established. Then, the substrate was heated rapidly to 800–900°C and the annealing step continued for 5 minutes. Next, CH<sub>4</sub> (>99.99%) or C<sub>2</sub>H<sub>2</sub> (>99.6%, dissolved in acetone) was used as the carbon source for graphene growth. The graphene growth duration was typically 10–120 seconds in a mixture of 50 sccm H<sub>2</sub> and 50 sccm CH<sub>4</sub> or C<sub>2</sub>H<sub>2</sub>. Upon completion of growth, the gas was switched to 200 sccm He and the substrate was rapidly cooled by turning off the heater power. An example program of temperature and gas flows is shown in Supplementary Fig. 2. As mentioned in the main text, the entire process was performed at 2 Torr (“low pressure”) or atmospheric pressure.

**Characterization.** Ni films were analyzed by scanning electron microscopy (FEI Helios Nanolab 650 Dualbeam Focused Ion Beam Workstation and Zeiss Supra55VP FESEM). Raman spectroscopy was performed using a 532 nm system (WITec alpha300 R). Optical microscopy was performed on a WITec alpha 300 R system. The graphene microstructure was characterized by atomic force microscopy (Veeco Dimension Icon) and transmission electron microscopy (JEOL 2100 and JEOL 2010 FEG-TEM). Plan view and cross sectional TEM specimens were prepared by conventional polishing followed by Argon ion milling. Alternatively, the graphene layers were transferred to lacey carbon TEM grids for plan view imaging. The respective top (before Ni delamination) and interfacial layers of graphene (after Ni delamination) were removed by scratching, dispersing them in acetone by sonication followed by drop casting on lacy carbon TEM grids. X-ray photoelectron spectroscopy was performed using a Physical Electronics Versaprobe II. The instrument used a scanning X-ray microprobe with a raster-scanned 10 μm diameter beam and pass energy 187.85 eV. The chamber pressure was 10–9 Torr.

- Zhang, Y., Zhang, L. & Zhou, C. Review of chemical vapor deposition of graphene and related applications. *Acc. Chem. Res.* **46**, 2329–2339 (2013).
- Kang, J., Shin, D., Bae, S. & Hong, B. H. Graphene transfer: Key for applications. *Nanoscale* **4**, 5527–5537 (2012).
- Regan, W. *et al.* A direct transfer of layer-area graphene. *Appl. Phys. Lett.* **96**, 113102 (2010).
- Pirkle, A. *et al.* The effect of chemical residues on the physical and electrical properties of chemical vapor deposited graphene transferred to SiO<sub>2</sub>. *Appl. Phys. Lett.* **99**, 122108 (2011).
- Bae, S. *et al.* Roll-to-roll production of 30-inch graphene films for transparent electrodes. *Nat. Nanotechnol.* **5**, 574–578 (2010).
- Allen, M. J. *et al.* Soft transfer printing of chemically converted graphene. *Adv. Mater.* **21**, 2098–2102 (2009).
- Suk, J. W. *et al.* Transfer of CVD-grown monolayer graphene onto arbitrary substrates. *ACS Nano* **5**, 6916–6924 (2011).
- Li, X. S. *et al.* Transfer of large-area graphene films for high-performance transparent conductive electrodes. *Nano Lett.* **9**, 4359–4363 (2009).
- Kim, C., Woo, J. Y., Choi, J., Park, J. & Han, C. S. Direct transfer of graphene without the removal of a metal substrate using a liquid polymer. *Scripta Mater.* **66**, 535–537 (2012).
- Ko, P. J. *et al.* Simple method to transfer graphene from metallic catalytic substrates to flexible surfaces without chemical etching. *J. Phys. Conf. Ser.* **433**, 012002 (2013).
- Kim, J. *et al.* Layer-resolved graphene transfer via engineered strain layers. *Science* **342**, 833–836 (2013).
- Peng, Z. W., Yan, Z., Sun, Z. Z. & Tour, J. M. Direct growth of bilayer graphene on SiO<sub>2</sub> substrates by carbon diffusion through nickel. *ACS Nano* **5**, 8241–8247 (2011).
- Yan, Z. *et al.* Growth of bilayer graphene on insulating substrates. *ACS Nano* **5**, 8187–8192 (2011).
- Wang, D. *et al.* Scalable and direct growth of graphene micro ribbons on dielectric substrates. *Sci. Rep.* **3**, 1348 (2013).
- Ismach, A. *et al.* Direct chemical vapor deposition of graphene on dielectric surfaces. *Nano Lett.* **10**, 1542–1548 (2010).
- van Laake, L., Hart, A. J. & Slocum, A. H. Suspended heated silicon platform for rapid thermal control of surface reactions with application to carbon nanotube synthesis. *Rev. Sci. Instrum.* **78**, 083901 (2007).
- Robinson, J. A. *et al.* Correlating Raman spectral signatures with carrier mobility in epitaxial graphene: A guide to achieving high mobility on the wafer scale. *Nano Lett.* **9**, 2873–2876 (2009).
- Rao, R. *et al.* Effects of layer stacking on the combination Raman modes in graphene. *ACS Nano* **5**, 1594–1599 (2011).
- Li, D. F. *et al.* Thickness and stacking geometry effects on high frequency overtone and combination Raman modes of graphene. *J. Raman Spectrosc.* **44**, 86–91 (2013).
- Cong, C. X., Yu, T., Saito, R., Dresselhaus, G. F. & Dresselhaus, M. S. Second-order overtone and combination Raman modes of graphene layers in the range of 1690–2150 cm<sup>-1</sup>. *ACS Nano* **5**, 1600–1605 (2011).
- Mohiuddin, T. M. G. *et al.* Uniaxial strain in graphene by Raman spectroscopy: G peak splitting, grüneisen parameters, and sample orientation. *Phys. Rev. B* **79**, 205433 (2009).





22. Yang, R., Shi, Z., Zhang, L., Shi, D. & Zhang, G. Observation of Raman G-Peak Split for Graphene Nanoribbons with Hydrogen-Terminated Zigzag Edges. *Nano Lett.* **11**, 4083–4088 (2011).
23. Caridad, J. M. *et al.* Effects of particle contamination and substrate interaction on the Raman response of unintentionally doped graphene. *J. Appl. Phys.* **108**, 205433 (2010).
24. Chae, S. J. *et al.* Synthesis of large-area graphene layers on poly-nickel substrate by chemical vapor deposition: wrinkle formation. *Adv. Mater.* **21**, 2328–2333 (2009).
25. Baskes, M. I. & Vitek, V. Trapping of hydrogen and helium at grain-boundaries in nickel - an atomistic study. *Metall. Trans. A* **16**, 1625–1631 (1985).
26. Trinkaus, H. On the modeling of the high-temperature embrittlement of metals containing helium. *J. Nucl. Mater.* **118**, 39–49 (1983).
27. Freund, L. B. & Suresh, S. *Thin film materials: stress, defect formation, and surface evolution.* (Cambridge University Press, Cambridge, England; New York; 2003).
28. Thompson, C. V. & Carel, R. Stress and grain growth in thin films. *J. Mech. Phys. Solids* **44**, 657–673 (1996).
29. Schroeder, H. & Ullmaier, H. Helium and hydrogen effects on the embrittlement of iron- and nickel-based alloys. *J. Nucl. Mater.* **179–181, Part 1**, 118–124 (1991).
30. Ishizaki, T., Xu, Q., Yoshiie, T., Nagata, S. & Troev, T. The effect of hydrogen and helium on microvoid formation in iron and nickel. *J. Nucl. Mater.* **307–311, Part 2**, 961–965 (2002).
31. Stamm, U. & Schroeder, H. The influence of helium on the high temperature mechanical properties of DIN 1.4914 martensitic steel. *J. Nucl. Mater.* **155–157, Part 2**, 1059–1063 (1988).
32. Bechtle, S., Kumar, M., Somerday, B. P., Launey, M. E. & Ritchie, R. O. Grain-boundary engineering markedly reduces susceptibility to intergranular hydrogen embrittlement in metallic materials. *Acta Mater.* **57**, 4148–4157 (2009).
33. Mittendorfer, F. *et al.* Graphene on Ni(111): Strong interaction and weak adsorption. *Phys. Rev. B* **84**, 201401 (2011).
34. Vanin, M. *et al.* Graphene on metals: A van der Waals density functional study. *Phys. Rev. B* **81**, 081408 (2010).
35. Zhiping Xu & Markus, J. B. Interface structure and mechanics between graphene and metal substrates: a first-principles study. *J. Phys.: Condens. Matter* **22**, 485301 (2010).
36. Myers, A. K., Schoofs, G. R. & Benziger, J. B. Comparison of benzene adsorption on nickel(111) and nickel(100). *J. Phys. Chem.* **91**, 2230–2232 (1987).
37. Jarvis, E. A. A. & Carter, E. A. Exploiting covalency to enhance metal–oxide and oxide–oxide adhesion at heterogeneous interfaces. *J. Am. Ceram. Soc.* **86**, 373–386 (2003).
38. Nguyen, T. C., Otani, M. & Okada, S. Semiconducting electronic property of graphene adsorbed on (0001) surfaces of SiO<sub>2</sub>. *Phys. Rev. Lett.* **106**, 106801 (2011).
39. Koenig, S. P., Boddeti, N. G., Dunn, M. L. & Bunch, J. S. Ultrastrong adhesion of graphene membranes. *Nat. Nanotechnol.* **6**, 543–546 (2011).
40. Zacharia, R., Ulbricht, H. & Hertel, T. Interlayer cohesive energy of graphite from thermal desorption of polyaromatic hydrocarbons. *Phys. Rev. B* **69**, 155406 (2004).
41. Rydberg, H. *et al.* Van der Waals density functional for layered structures. *Phys. Rev. Lett.* **91**, 126402 (2003).
42. Lu, N. S., Wang, X., Suo, Z. G. & Vlassak, J. Failure by simultaneous grain growth, strain localization, and interface debonding in metal films on polymer substrates. *J. Mater. Res.* **24**, 379–385 (2009).
43. Hutchinson, J. W. Mixed mode cracking in layered materials. *Adv. Appl. Mech.* **29**, 191 (1992).
44. Nessim, G. D. *et al.* Synthesis of tall carpets of vertically aligned carbon nanotubes by in situ generation of water vapor through preheating of added oxygen. *Carbon* **50**, 4002–4009 (2012).

## Acknowledgments

Primary financial support (to D.Q.M., B.V., F.L., and A.J.H.) was provided by Guardian Industries. Additional support was provided by the NSF Scalable Nanomanufacturing Program (to F.L., E.S.P.; DMR-1120187), the Air Force Office of Scientific Research (to D.C.; FA9550-11-1-0089), and the NSF Graduate Research Fellowship Program (to C.G.P. and N.T.D.). Work was performed in part at the University of Michigan Electron Microbeam Analysis Library (EMAL), the University of Michigan Lurie Nanofabrication Facility (LNF), the Harvard Center for Nanoscale Systems (CNS), and the MIT Center for Materials Science and Engineering (CMSE). The LNF and CNS are members of the National Nanotechnology Infrastructure Network (NNIN), which is supported by the National Science Foundation (NSF). We thank Prof. Michael Thouless (University of Michigan) for discussions on thin film mechanics, Asish Misra and Prof. Joerg Lahann (University of Michigan) for assistance with 2-D Raman spectroscopy, and Sebastian Pattinson (MIT) for performing the XPS analysis.

## Author contributions

A.J.H., D.Q.M., B.V., V.S.V. and D.C. designed research, which was supervised by A.J.H.; D.Q.M., B.V., F.R.L., N.T.D. and D.C. fabricated Ni and graphene films; D.Q.M. performed optical microscopy and Raman spectroscopy; D.Q.M. and E.S.P. performed atomic force microscopy; B.V., F.R.L., D.Q.M., N.T.D. and E.S.P. performed scanning electron microscopy; B.V. performed transmission electron microscopy; B.V., C.P., A.C.B., D.C. and V.S.V. performed Ni film stress modeling and calculations; D.Q.M., B.V., C.P. and A.J.H. wrote the manuscript, with input from V.S.V. All authors discussed the results and reviewed and commented on the manuscript.

## Additional information

**Supplementary information** accompanies this paper at <http://www.nature.com/scientificreports>

**Competing financial interests:** The University of Michigan and Guardian Industries have jointly filed a patent application including the findings of this study.

**How to cite this article:** McNerny, D.Q. *et al.* Direct fabrication of graphene on SiO<sub>2</sub> enabled by thin film stress engineering. *Sci. Rep.* **4**, 5049; DOI:10.1038/srep05049 (2014).



This work is licensed under a Creative Commons Attribution-NonCommercial-ShareAlike 3.0 Unported License. The images in this article are included in the article's Creative Commons license, unless indicated otherwise in the image credit; if the image is not included under the Creative Commons license, users will need to obtain permission from the license holder in order to reproduce the image. To view a copy of this license, visit <http://creativecommons.org/licenses/by-nc-sa/3.0/>